

Multi-reference quantum chemistry protocol for simulating autoionization spectra: Test of ionization continuum models for the neon atom

Gilbert Grell, Oliver Kühn, and Sergey I. Bokarev*

Institut für Physik, Universität Rostock, Albert-Einstein-Str. 23-24, 18059 Rostock, Germany

(Dated: December 15, 2024)

In this contribution we present a protocol to evaluate partial and total Auger decay rates combining the restricted active space self-consistent field electronic structure method for the bound part and numerically obtained continuum orbitals in the single-channel scattering theory framework. On top of that, the two-step picture is employed to evaluate the partial rates. The performance of the method is exemplified for the prototypical Auger decay of the neon $1s^{-1}3p$ resonance. Different approximations to obtain the continuum orbitals, the partial rate matrix elements, and the electronic structure of the bound part are tested against theoretical and experimental reference data. It is demonstrated that the partial and total rates are most sensitive to the accuracy of the continuum orbital. For instance, it is necessary to account for the true direct Coulomb potential of the ion for the determination of the continuum wave functions. The Auger energies, however, can be reproduced quite well already with a rather small active space. Finally, perspectives of the application of the proposed protocol to molecular systems are discussed.

I. INTRODUCTION

Ionization triggered by photon absorption occurs along two pathways. In direct photoionization, the energy is transferred to an ejected electron. Alternatively, the system can be first put into a metastable state by a resonant excitation and afterwards decay via an autoionization mechanism. Autoionization can be approximately understood as a two-step process [1], in which the decay can be considered independently from the excitation process and interferences between direct and autoionization are neglected. For example, let us consider an atomic species, such as a neon atom that is prepared in a highly excited state $|\Psi_i\rangle$ above the continuum threshold at $E = 0$ eV, Fig. 1. This state spontaneously decays into the continuum state $|\Psi_\alpha\rangle$ comprising the discrete state $|\Psi_f^+\rangle$ of the ion and the emitted electron, $|\psi_\alpha\rangle$, carrying the excess energy $\varepsilon_\alpha = \mathcal{E}_i - \mathcal{E}_f$. The system's electronic structure is thus encoded into the kinetic energy spectrum of the ionized electrons. Photoelectron Spectroscopy (PES) and Autoionization Spectroscopy (AIS) map bound states to the continuum which makes them less sensitive to selection rule suppression and more informative than spectroscopies involving optical transitions between bound states [2–4].

Autoionization processes, predominantly Auger decay [5], but also Interatomic Coulombic Decay (ICD) [6] and Electron Transfer Mediated Decay (ETMD) [7] are particularly interesting on their own. Due to their correlated nature, they not only probe but also initiate or compete with intricate ultrafast electronic and nuclear dynamics e.g. [8–12]. Additionally, they provide the main channel for the decay of core vacancies [13] and play a key role in biological radiation damage, creating

highly charged cations while a cascade of highly reactive low energy electrons is emitted [11, 14–17]. Further, in free electron laser experiments operating with ultrashort intense X-ray pulses, autoionization after multiple photoionization induces the Coulomb explosion of the target, which limits the achievable spectroscopic and temporal resolution [18]. Due to this wealth of applications, autoionization and especially the local Auger effect have been studied extensively both theoretically and experimentally since its discovery by Meitner [5] and description by Wentzel [1].

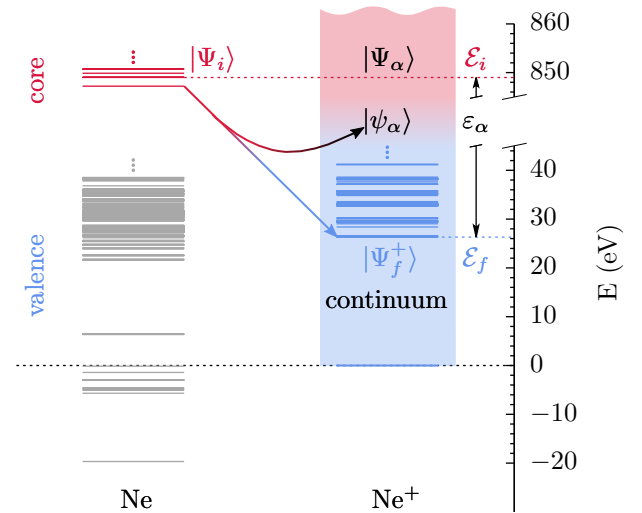


Figure 1. Autoionization scheme for the neon atom. The core vacancy state $|\Psi_i\rangle$ with energy \mathcal{E}_i (red) decays isoenergetically into the continuum state $|\Psi_\alpha\rangle$ (black) composed of the ionic bound state $|\Psi_f^+\rangle$ with energy \mathcal{E}_f (blue) and the continuum orbital $|\psi_\alpha\rangle$ of the outgoing electron with the excess energy ε_α . States that do not contribute to the process are depicted in gray; the singly ionized continuum is denoted by the color gradient.

* sergey.bokarev@uni-rostock.de

Remarkably, AIS simulations of molecular systems remain challenging until today, although the fundamental theory is known for decades [19–21]. For atoms, methods combining highly accurate four-component Multi-configurational Dirac-Fock (MCDF) calculations with multichannel scattering theory are publicly available [22], whereas no such general purpose code exists for molecules. The main complication of the molecular case lies in the construction of molecular continuum states $|\Psi_\alpha\rangle$. The approaches to the simulation of AIS published during the last decades can be classified into two families – those that circumvent the continuum orbital problem and those that treat the continuum orbital explicitly.

The first family comprises the following flavors: The simplest method that allows to assign experimental AIS is to evaluate the energetic peak positions [23–25]. On top of that simple estimates for the partial decay rates can be obtained based on an electron population analysis [26]. More advanced approaches rely on an implicit continuum representation with Stieltjes imaging [27], a Green’s operator [28, 29], or a propagator [30, 31] formalism. From this group, the Fano-Stieltjes Algebraic Diagrammatic Construction (Fano-ADC) method [32] has been used to evaluate Auger, ICD and ETMD decay rates of van der Waals clusters [33], first row hydrides [34] and the $[\text{Mg}(\text{H}_2\text{O})_6]^{2+}$ cluster [11]. However, this approach cannot describe the angular distribution of the outgoing electron and relies on an ad-hoc procedure to evaluate partial decay rates.

The second family, relying on an explicit representation of the continuum wave function, consists of the following approaches: The one-center approximation uses atomic continuum functions centered at the vacancy-bearing atom to describe the outgoing electron in the evaluation of partial decay rates [35–38]. This approximation can be applied on top of high-level electronic structure methods [39]. It is also applied in the XMOLECULE package [40, 41] which is based on very cost efficient but simplistic electronic structure calculations, which allows the evaluation of ionization cascades but may limit the applicability for complex molecules. Further, the influence of the molecular field may be taken into account perturbatively [42, 43] or in a complete manner with, e.g., the single-center approach, where the whole molecular problem is projected onto a single-centered basis [44–46].

Finally, multi-channel scattering theory methods that combine finite multi-centered basis sets with the appropriate boundary conditions to represent the molecular continuum have been developed [47] and applied to the AIS of a variety of small systems [47–49]. For instance, the recently developed XCHEM approach [50] has been applied to simulate PES and AIS of atoms [51] and small molecular systems [52]. These techniques represent the most general and accurate quantum-mechanical treatment of the problem, thus potentially serving as a high-level reference, although connected to substantial computational effort.

Summarizing, most of the mentioned methods have been applied only to simple diatomics, first row hydrides, halogen hydrides, and small molecules consisting of not more than two heavy atoms. Studies of larger molecular systems, such as tetrahedral molecules, small aldehydes, and amides [53, 54], solvated metal ions [11] and polymers [55] are very scarce. In fact, the Fano-ADC [32, 33] and the XMOLECULE [40, 41] approaches are the only publicly available tools that allow to simulate AIS for a variety of systems without restricting the molecular geometry. Further, both methods are not suited to treat systems possessing multi-configurational wave functions. This puts studies of some chemically interesting systems having near-degeneracies, for example, transition metal compounds, or of photodynamics in the excited electronic states, e.g., near conical intersections, out of reach. To keep up with the experimental advancements, the development of a general purpose framework to evaluate autoionization decay rates (Auger, ICD, and ETMD) for molecular systems is warrant. Such a framework should be kept accessible, transferable and easy to use, i.e. it should be based on widespread robust and versatile Quantum Chemistry (QC) methods.

Here, we present a protocol that combines multi-configurational Restricted Active Space (RAS) Self-Consistent Field (SCF) (RASSCF) bound state wave functions with single-centered numerical continuum orbitals in the single-channel scattering theory framework [56]. We have chosen the RASSCF approach, since it is known to yield reliable results for core-excited states, needed in the simulation of X-ray absorption [57, 58], resonant inelastic scattering [59, 60], and photoemission spectra [61–63] suggesting its application to AIS.

Although the ultimate goal is to investigate molecules, this proof-of-concept contribution focuses on the simulation of the prototypical neon $1s^{-1}3p$ Auger Electron Spectrum (AES) to calibrate the approach, since highly accurate reference data are available for both theory [64] and experiment [65–68]. Special attention is paid to the representation of the radial continuum waves, which is investigated herein by a thorough test of different approximations. Note that our implementation allows to calculate molecular AIS as well as PES which will be presented elsewhere.

We commence this article with an introduction to the underlying theory and further give important details of our implementation. It continues with the computational details and the benchmark of our results against theoretical and experimental references. Finally, we conclude the discussion and present perspectives for the molecular application.

II. THEORY

The approach for the calculation of partial autoionization rates comprises the following approximations:

- (i) The two-step model [1] is employed, i.e., excitation

and decay processes are assumed to be decoupled and interference effects between photoionization and autoionization are neglected, Fig. 1. Within this approximation, the partial autoionization rate for the decay $i \rightarrow \alpha$ reads [19]

$$\Gamma_{i\alpha} = 2\pi |\langle \Psi_\alpha | \mathcal{H} - \mathcal{E}_i | \Psi_i \rangle|^2. \quad (1)$$

Atomic units are used everywhere, unless explicitly stated otherwise.

(ii) We require that all bound state wave functions have the form of Configuration Interaction (CI) expansions in terms of N -electron Slater determinants $|\Theta_j\rangle$:

$$|\Psi\rangle = \sum_j C_j |\Theta_j\rangle, \quad (2)$$

$$|\Theta_j\rangle = \hat{A}^- |\varphi_{j_1, \sigma_1} \cdots \varphi_{j_N, \sigma_N}\rangle = a_{j_1, \sigma_1}^\dagger \cdots a_{j_N, \sigma_N}^\dagger |0\rangle. \quad (3)$$

The a_{i, σ_i}^\dagger are the usual fermionic creation operators in the spin-orbital basis $\{\varphi_{i, \sigma_i}\}$ and \hat{A}^- is the antisymmetrization operator. In this work, multi-configurational bound state wave functions for the unionized and ionized states $|\Psi_i\rangle$ and $|\Psi_f^+\rangle$ are obtained with the RASSCF or Restricted Active Space Second-order Perturbation Theory (RASPT2) method. However, the presented protocol can employ any CI-like QC method.

(iii) The limit of weak relativistic effects is assumed, thus the total spins S, S^+ and their z -axis projections M, M^+ of the bound unionized and ionized system are good quantum numbers. Further, S and M of the unionized species are conserved during the process.

(iv) The single-channel scattering theory framework is employed, disregarding interchannel coupling, as well as correlation effects between the bound and outgoing electrons.

(v) The continuum orbitals are treated as spherical waves, subject to the spherically averaged potential $V_f(r)$ of the ionic state $|\Psi_f^+\rangle$. Hence, the continuum orbitals have the form

$$\psi_{\alpha, \sigma}(r, \vartheta, \phi) = \frac{1}{r} w_l^{fk}(r) Y_l^m(\vartheta, \phi) \zeta(\sigma), \quad (4)$$

with spherical harmonics $Y_l^m(\vartheta, \phi)$ being the angular part and $\zeta(\sigma)$ the spin function. For brevity, $\zeta(\sigma)$ is generally omitted and present only when needed. The composite channel index $\alpha = (f, l, m, k)$ contains the index of the ionized state f , the orbital and magnetic quantum numbers l, m and the wave number $k = \sqrt{2\varepsilon_\alpha}$ of the continuum orbital. This notation uniquely identifies the total energy $\mathcal{E}_\alpha = \mathcal{E}_f + \varepsilon_\alpha$, the continuum orbital and bound state for each channel $|\Psi_\alpha\rangle$. Generally, indices i and f always refer to bound states of the unionized and ionized species and α denotes decay channels.

The radial part $w_l^{fk}(r)/r$ is determined by solving the

radial Schrödinger equation

$$\left(\frac{d^2}{dr^2} + 2 \left(\frac{k^2}{2} - V_f(r) \right) - \frac{l(l+1)}{r^2} \right) w_l^{fk}(r) = 0. \quad (5)$$

With the assumptions (i)-(v), the N -electron ionized continuum states with conserved total spin and projection of the unionized states, S and M , can be written as:

$$|\Psi_\alpha\rangle = \sum_{M^+ = -S^+}^{S^+} \sum_{\sigma = -\frac{1}{2}, \frac{1}{2}} C_{S^+, M^+; \sigma}^{S, M} |\Upsilon_\alpha^{M^+, \sigma}\rangle, \quad (6)$$

where σ is the spin projection of the outgoing electron. The Clebsch-Gordan coefficients $C_{S^+, M^+; \sigma}^{S, M} = \langle S, M | S^+, M^+; \frac{1}{2}, \sigma \rangle$ couple the channel functions $|\Upsilon_\alpha^{M^+}\rangle$. These are constructed by inserting an additional electron with the continuum orbital $|\psi_{\alpha, \sigma}\rangle$ into the bound ionic state with spin projection M^+ , retaining the anti-symmetry:

$$|\Upsilon_\alpha^{\sigma M^+}\rangle = a_{\alpha, \sigma}^\dagger |\Psi_{f, M^+}^+\rangle. \quad (7)$$

Note that in contrast to the continuum state $|\Psi_\alpha\rangle$ which is an eigenstate of \mathbf{S}^2 and S_z , the $|\Upsilon_\alpha^{\sigma M^+}\rangle$ are not eigenfunctions of \mathbf{S}^2 , but only of S_z .

III. DETAILS OF THE IMPLEMENTATION

A. Model potentials

We commence with the discussion of different approximations to the potential $V_f(r)$ in Eq. (5) which are central for the quality of the free electron function. In this work, we have used the following models:

$$V_f^{\text{free}} = 0, \quad (8a)$$

$$V_f^{\text{eff}}(r) = -\frac{Z_{\text{eff}}}{r}, \quad (8b)$$

$$V_f^{\text{scr}}(r) = -\frac{Z_f(r)}{r}, \quad (8c)$$

$$V_f^{\text{J}}(r) = V_{\text{nuc}}(r) + J_f(r), \quad (8d)$$

$$V_f^{\text{JX}}(r) = V_{\text{nuc}}(r) + J_f(r) + X_f^{\text{S}}(r). \quad (8e)$$

In other words, we use (a) no potential; (b) an effective Coulomb potential with a fixed variable charge Z_{eff} ; (c) the screened Coulomb potential of an ionic state f with the charge $Z_f(r)$; (d) the spherically averaged direct nuclear and electronic potentials of the ionic state, $V_{\text{nuc}}(r)$ and $J_f(r)$, respectively, see below; (e) the potential of (d) augmented with Slater's exchange term $X_f^{\text{S}}(r)$ [69]. For the state-dependent models (c-e), the central quantity is

the spherically-averaged electron density of the ionized state

$$\rho_f(r) = \frac{1}{4\pi} \int_0^{4\pi} \rho_f(\mathbf{r}) d\Omega. \quad (9)$$

It determines the potentials in the following way: The screened charge $Z_f(r)$ in (c) is evaluated as the difference between the nuclear charge Z and the integrated number of electrons present in a sphere with radius r around the atom:

$$Z_f(r) = Z - \int_0^r \rho_f(r') r'^2 dr'. \quad (10)$$

Further, the direct Coulomb potential of the ionized states in (d) and (e) is found by solving Maxwell's equation for the electrostatic potential of the spherically averaged electron density $\rho_f(r)$ with the usual boundary conditions,

$$J_f(r) = J_f(0) - \frac{4\pi}{r} \int_0^r dr' \int_0^{r'} r'' \rho_f(r'') dr''. \quad (11)$$

$J_f(0)$ is defined by the asymptotic value of the integral over r'' in Eq. (11):

$$\frac{J_f(0)}{4\pi} = \lim_{r' \rightarrow \infty} \int_0^{r'} r'' \rho_f(r'') dr''. \quad (12)$$

Finally, a radial Slater type exchange [69],

$$X_f^S(r) = -3 \left(\frac{3}{8\pi} \rho_f(r) \right)^{-\frac{1}{3}}, \quad (13)$$

is employed.

B. Continuum Orbital

The solutions to the radial Schrödinger equation, Eq. (5), using the potentials (8a)–(8e) can be understood as follows: In (a), assuming a free particle, we completely neglect any influence of the ion onto the outgoing electron. Here, the radial part of $\psi_{\alpha,\sigma}(r, \vartheta, \varphi)$ corresponds to spherical Bessel functions $j_l(kr)$ [70]:

$$\psi_{\alpha,\sigma}^{\text{free}}(r, \vartheta, \phi) = \sqrt{\frac{2}{\pi}} k \cdot j_l(kr) Y_l^m(\vartheta, \phi) \zeta(\sigma) \quad (14)$$

The prefactor $\sqrt{\frac{2}{\pi}} k$ ensures the correct normalization,

$$\langle \psi_{\alpha,\sigma} | \psi_{\alpha',\sigma'} \rangle = \delta_{ll'} \delta_{m_l m_l'} \delta_{\sigma\sigma'} \delta(k - k'), \quad (15)$$

which is exact only for the free particle approach, and approximate for all other potentials, due to the long range Coulomb distortion.

Modeling the ionic potential in an effective Coulomb form, (b) is the simplest approach to approximately account for the ionic potential. It has the advantage that the solutions to Eq. (5) are still analytically available in the form of regular Coulomb functions F_l [70]:

$$\psi_{\alpha,\sigma}^{\text{eff}}(r, \vartheta, \phi) = \sqrt{\frac{2}{\pi}} \cdot \frac{F_l(\eta, kr)}{r} Y_l^m(\vartheta, \phi) \zeta(\sigma), \quad (16)$$

with $\eta = -Z_{\text{eff}}/2k$.

The approaches (c-e) yield numerically obtained potentials according to Eqs. (8c)–(8e) and thus require a numerical solution of the radial Schrödinger equation. Asymptotically, the numerical radial waves satisfy the boundary conditions:

$$w_l^{fk}(r \rightarrow 0) = nr^{l+1}, \quad (17a)$$

$$w_l^{fk}(r \rightarrow \infty) = \sqrt{\frac{2}{\pi}} \left(\cos \delta_l^f(k) F_l(\eta, kr) + \sin \delta_l^f(k) G_l(\eta, kr) \right). \quad (17b)$$

The scaling factors and phase shifts $\delta_l^f(k)$ are obtained by matching the numerical solutions and their first derivatives with a linear combination of the regular and irregular Coulomb functions F_l and G_l , [70]. This matching is carried out in the asymptotic region where the potential is well approximated by the Coulomb potential of the ions net charge $V_f(r) \approx -Z_{\text{net}}/r$. This description may be straightforwardly expanded to ingoing wave boundary conditions that are usually employed for ionization processes in the framework of scattering theory. Doing so is needed to allow for the treatment of photoelectron angular distributions and angular resolved spectra, which we neglect in this contribution.

Since the screened Coulomb potential model, Eq. (8c) is an ad-hoc assumption based on the simple idea that the nuclear charge is screened by the integrated electron density, the applicability of this model needs to be tested. In turn, (d) and (e), employing the spherically averaged direct Coulomb and exchange terms according to Eqs. (8d) and (8e), in a sense correspond to the Hartree and Hartree-Fock levels of accuracy, respectively. Note that no iterative SCF procedure is performed in the construction of the continuum functions. Therefore, correlation and non-local exchange effects between the continuum orbital and the bound part are neglected in all the discussed models.

The continuum orbitals evaluated using any of the methods presented in the preceding section are not orthogonal to the orbitals of the bound ionic state $\langle \psi_{\alpha,\sigma} | \varphi_{i,\sigma_i} \rangle \neq 0$, which is in contrast to the behavior that an exact continuum orbital would possess.

C. Continuum matrix elements

Using the decomposition of the continuum states in terms of channel functions in Eq. (6), the partial rate

expression in Eq. (1) reads:

$$\Gamma_{i\alpha} = 2\pi \left| \sum_{M^+, \sigma} C_{S^+, M^+; \sigma}^{S, M} \langle \Upsilon_{\alpha}^{\sigma M^+} | \mathcal{H} - \mathcal{E}_i | \Psi_i \rangle \right|^2 \quad (18)$$

Decomposing the Hamiltonian \mathcal{H} into the one and two-electron parts $\mathcal{H} = \sum_u h_u + \sum_{u < v} 1/r_{uv}$, the following matrix elements need to be evaluated between bound states and channel functions:

$$\Gamma_{i\alpha} = 2\pi \left| \sum_{M^+, \sigma} C_{S^+, M^+; \sigma}^{S, M} \left[\sum_u \langle \Upsilon_{\alpha}^{\sigma M^+} | h_u | \Psi_i \rangle + \sum_{u < v} \langle \Upsilon_{\alpha}^{\sigma M^+} | \frac{1}{r_{uv}} | \Psi_i \rangle - \mathcal{E}_i \langle \Upsilon_{\alpha}^{\sigma M^+} | \Psi_i \rangle \right] \right|^2 \quad (19)$$

The expressions for the overlap, one- and two-electron matrix elements in Eq. (19) are obtained by using Löwdins Slater determinant calculus [71]. Here one has to take into account that the unionized and ionized bound states are obtained in separate SCF calculations. Consequently, they have different sets of N_{orb} spin-orbitals $\{\varphi_i\}$ and $\{\varphi_i^+\}$ that are not mutually orthogonal. The spin coordinates are implicitly assumed to be assigned as introduced in Eq. (3). Then, the respective creation and annihilation operators are a_i^\dagger , a_i and $(a_i^+)^{\dagger}$, a_i^+ .

With this, the overlap integral in Eq. (19) can be rearranged into the overlap of the continuum orbital and the Dyson Orbital (DO) $|\Phi_{i\alpha}^{M^+}\rangle$,

$$\langle \Upsilon_{\alpha}^{\sigma M^+} | \Psi_i \rangle = \langle \psi_{\alpha, \sigma} | \Phi_{i\alpha}^{M^+} \rangle. \quad (20)$$

The DO is generally defined as the $N-1$ particle integral over the transition density of the unionized and ionized states $|\Psi_i\rangle$ and $|\Psi_{f, M^+}^+\rangle$ that are associated with the channel α

$$\Phi_{i\alpha}^{M^+}(\mathbf{x}) = \sqrt{N} \int \left(\Psi_{f, M^+}^+(\{\mathbf{x}_{N-1}\}) \right)^* \Psi_i(\{\mathbf{x}_N\}) d\{\mathbf{x}_{N-1}\}, \quad (21)$$

and can be expressed in second quantization as a linear combination of the spin-orbitals $\{\varphi_s\}$ of the unionized species, with the coefficients $\phi_{\alpha, s}^{M^+}$

$$|\Phi_{i\alpha}^{M^+}\rangle = \sum_{s=1}^{N_{\text{orb}}} \underbrace{\langle \Psi_{f, M^+}^+ | a_s | \Psi_i \rangle}_{\phi_{\alpha, s}^{M^+}} |\varphi_s\rangle. \quad (22)$$

Staying on this route, the one-electron transition matrix elements in Eq.(19) are

$$\begin{aligned} \sum_u \langle \Upsilon_{i\alpha}^{M^+, \sigma} | h_u | \Psi_i \rangle &= \langle \psi_{\alpha, \sigma} | h | \Phi_{i\alpha}^{M^+} \rangle \\ &+ \sum_{q=1}^{N_{\text{orb}}} \langle \varphi_q^+ | h | \tilde{\Phi}_{i\alpha}^{\sigma M^+, q} \rangle, \end{aligned} \quad (23)$$

where the second term with the conjugated Dyson orbital,

$$|\tilde{\Phi}_{i\alpha}^{\sigma M^+, q}\rangle = \sum_{s=1}^{N_{\text{orb}}} \underbrace{\langle \Upsilon_{\alpha}^{\sigma M^+} a_q^{\dagger} | a_s | \Psi_i \rangle}_{\tilde{\phi}_{\alpha, s}^{\sigma M^+, q}} |\varphi_s\rangle, \quad (24)$$

arises due to the nonorthogonality of the continuum orbital and the orbitals of the unionized system. The two-electron matrix elements can be formulated in a similar way:

$$\begin{aligned} \sum_{u < v} \langle \Upsilon_{\alpha}^{\sigma M^+} | \frac{1}{r_{uv}} | \Psi_i \rangle &= \sum_{q=1}^{N_{\text{orb}}} \langle \psi_{\alpha, \sigma} \varphi_q^+ | \frac{1}{r_{12}} | \Xi_{i\alpha}^{M^+, q} \rangle \\ &+ \sum_{q_1 < q_2}^{N_{\text{orb}}} \langle \varphi_{q_1}^+ \varphi_{q_2}^+ | \frac{1}{r_{12}} | \tilde{\Xi}_{i\alpha}^{\sigma M^+, q_1 q_2} \rangle. \end{aligned} \quad (25)$$

The quantities $|\Xi_{i\alpha}^{M^+, q}\rangle$ and $|\tilde{\Xi}_{i\alpha}^{\sigma M^+, q_1 q_2}\rangle$ are the two-electron and conjugated two-electron reduced transition densities. They are linear combinations of pairs of the unionized orbitals with the coefficients $\xi_{i\alpha, s_1 s_2}^{M^+, q}$ and $\tilde{\xi}_{i\alpha, s_1 s_2}^{\sigma M^+, q_1 q_2}$:

$$|\Xi_{i\alpha}^{M^+, q}\rangle = \sum_{s_1 < s_2}^{N_{\text{orb}}} \underbrace{\langle \Psi_{f, M^+}^+ (\hat{a}_q^+)^{\dagger} | \hat{a}_{s_1} \hat{a}_{s_2} | \Psi_i \rangle}_{\xi_{i\alpha, s_1 s_2}^{M^+, q}} |\varphi_{s_1} \varphi_{s_2}\rangle \quad (26)$$

$$\begin{aligned} |\tilde{\Xi}_{i\alpha}^{\sigma M^+, q_1 q_2}\rangle &= \sum_{s_1 < s_2}^{N_{\text{orb}}} \underbrace{\langle \Upsilon_{\alpha}^{\sigma M^+} (\hat{a}_{q_1}^+)^{\dagger} (\hat{a}_{q_2}^+)^{\dagger} | \hat{a}_{s_1} \hat{a}_{s_2} | \Psi_i \rangle}_{\tilde{\xi}_{i\alpha, s_1 s_2}^{\sigma M^+, q_1 q_2}} \\ &\times |\varphi_{s_1} \varphi_{s_2}\rangle \end{aligned} \quad (27)$$

Notice that if the Strong Orthogonality (SO) approximation is implied, the “conjugate” quantities $|\tilde{\Phi}_{i\alpha}^{\sigma M^+, q}\rangle$ and $|\tilde{\Xi}_{i\alpha}^{\sigma M^+, q_1 q_2}\rangle$ (Eq. (24) and (27)) disappear. Thus, assuming SO substantially simplifies the computation since the evaluation of the “conjugate” terms is notably more involved. A similar effect is achieved by using the Gram-Schmidt (GS) orthogonalization to enforce orthogonality of the continuum and bound orbitals:

$$|\psi_{\alpha, \sigma}^{\text{GS}}\rangle = |\psi_{\alpha, \sigma}\rangle - \sum_{i=1}^{N_{\text{orb}}} \langle \varphi_i^+, \sigma_i | \psi_{\alpha, \sigma} \rangle |\varphi_i^+, \sigma_i\rangle \quad (28)$$

This approach has been tried before, e.g., in Ref. 44 and will be tested herein as well.

In the following, we will use the labels SO, NO and GS to indicate that the conjugate terms have been neglected

(SO), fully included (NO), and that the GS procedure has been used to evaluate the partial rates. Further, we also compare the results of the “full” Hamiltonian coupling, against the popular choice to account only for the two-electron terms in Eq. (19), denoting them as \mathcal{H} and r^{-1} coupling, respectively.

To sum up, the present article reports on the influence of different combinations of the introduced approximations to the potentials, transition matrix elements, and continuum orbitals on the partial Auger decay rates of the exemplary neon $1s^{-1}3p$ resonance. As a shorthand notation for the combination of the different approximations we will use the *coupling · potential · nonorthogonality* notation, were applicable. For instance, $\mathcal{H} \cdot V_f^{\text{JX}}(r) \cdot \text{NO}$ denotes partial rates obtained using the \mathcal{H} coupling, with radial waves corresponding to the $V_f^{\text{JX}}(r)$ potential including the conjugate terms.

IV. COMPUTATIONAL DETAILS

A. Quantum chemistry for bound states

The wave functions of the bound neutral and ionic states have been obtained in separate state-averaged RASSCF calculations with a locally modified version of MOLCAS 8.0 [72]. To prevent mixing of different angular momentum basis functions into one orbital, the “atom” keyword has been employed. The QC schemes used to evaluate the bound states $|\Psi_i\rangle$ and $|\Psi_f^+\rangle$ are presented in Table I. The RAS formalism is a flexible means to select

QC	Basis Set	Active Space (AS)	States Ne/Ne ⁺	X2C
I	[7s6p3d2f]	RAS(8; 1, 1)	41/132	no
II	[22s6p3d2f]-rcc	RAS(8; 1, 1)	41/132	yes
III	[9s8p5d4f]	RAS(26; 1, 1)	131/420	no

Table I. QC setups and number of states used in the state-averaged RASSCF calculations

electronic configurations. Therein, the AS is subdivided into three subspaces RAS1, RAS2 and RAS3. The RAS notation that is used throughout the paper is to be understood as follows: In all spaces, the $1s$ orbital forms the RAS1 subspace and the $2s$ and $2p$ orbitals build up the RAS2 one. The occupation of the $2s$ and $2p$ orbitals in RAS2 is not restricted, while only h electrons may be removed from RAS1. Finally the RAS3 subspace contains v virtual orbitals that can be occupied by at most p electrons. Thus, we can herein uniquely specify each AS as RAS($v; h, p$). The ASs used in this study are: RAS(8; 1, 1), containing $3s$, $3p$, $4s$, and $4p$ orbitals in the RAS3; RAS(26; 1, 1), enlarging RAS3 by the $3d$, $4d$, $5s$, $5p$, $6s$, and $6p$ orbitals and RAS(33; 1, 1), adding the $4f$ orbitals. The number of configurations possible with each AS is shown in Table II. For all QC schemes

RAS	RAS(8; 1, 1)	RAS(8; 26, 1)	RAS(8; 33, 1)
Ne	41	131	166
Ne ⁺	197	629	797

Table II. Maximum number of configurations for each AS

(see Table I) all states are included in the RASSCF procedure for the Ne wave functions, while the core excited states have been excluded for the calculations of Ne⁺.

Atomic Natural Orbital (ANO) type basis sets have been employed using a (22s17p12d11f) primitive set. It was constructed by supplementing the ANO exponents for neon [73] in each angular momentum with eight Rydberg exponents generated according to the scheme proposed by Kaufmann et al. [74]. The contractions were then obtained with the GENANO module [75] of OpenMolcas [76] using density matrices from state averaged RASSCF calculations for Ne and Ne⁺ with the RAS(33; 1, 1) AS. All possible 166 states for Ne have been taken into account but for Ne⁺, the core excited manifold has been excluded, leading to 532 states. To get the final basis set, the sets obtained for Ne and Ne⁺ have been evenly averaged. In this work, we use the contractions: [7s6p3d2f], obtained by the procedure described above; [9s8p5d4f], corresponding to [7s6p3d2f] supplemented with Rydberg contractions that resulted from the GENANO procedure using the “rydberg” keyword; [22s6p3d2f]-rcc, similiar to [7s6p3d2f] but with uncontracted s functions and scalar relativistic corrections according to the Exact Two Component Decoupling (X2C) scheme [77].

All energies have been corrected using the single state RASPT2 method [78] with an imaginary shift of 0.01 a.u. The RAS State Interaction (RASSI) [79] module of MOLCAS was used to compute the biorthonormally transformed orbital and CI coefficients [80] for the atomic and ionic states: $\{\varphi_i\}, \{C_j\} \rightarrow \{\tilde{\varphi}_i\}, \{\tilde{C}_j\}$ such that $\langle \tilde{\varphi}_i^+ | \tilde{\varphi}_j \rangle = \delta_{ij}$, while the total wave functions remain unchanged. This biorthonormal basis is used in the evaluation of the Dyson orbitals, Eqs. (22), (24), and two-electron reduced transition densities, Eqs. (26), (27).

B. Matrix elements in the atomic basis

The matrix elements between bound orbitals occurring in Eqs (19, 23, 25) are evaluated by transforming the orbitals to the atomic basis and calculating the atomic basis integrals with the libcint library [81]. The most time consuming part in the computation of the partial decay rates using Eq. (19) is the estimation of the two-electron continuum-bound integrals. Transforming the two-electron reduced transition densities and the orbitals to the atomic basis $\{\chi_i\}$ and neglecting the spin integration, the two-electron continuum-bound integrals $\langle \psi_\alpha \chi_a | \frac{1}{r_{12}} | \chi_b \chi_c \rangle = (aa|bc)$ used in the practical evalua-

tion of Eq. (25) read as:

$$(\alpha a|bc) = \int \psi_\alpha^*(\mathbf{r}_1) \chi_b(\mathbf{r}_1) \underbrace{\left[\int \frac{\chi_a^*(\mathbf{r}_2) \chi_c(\mathbf{r}_2)}{r_{12}} d\mathbf{r}_2 \right]}_{f_{ac}(\mathbf{r}_1)} d\mathbf{r}_1^3. \quad (29)$$

The function $f_{ac}(\mathbf{r}_1)$ is similar to an atomic nuclear attraction integral, and is evaluated as a function of \mathbf{r}_1 using the libcint library [81]. An important point is to exploit the fact that the kinetic energy of the continuum electron is only encoded in its radial part. Transforming to spherical coordinates $\mathbf{r} \rightarrow (r, \Omega)$ centered at the origin of the outgoing electron allows to separate off the radial integration:

$$(\alpha a|bc) = \int_0^\infty r w_l^{fk}(r) \times \underbrace{\left[\int_\Omega Y_l^m(\Omega) \chi_b(\mathbf{r}(r, \Omega)) f_{ac}(\mathbf{r}(r, \Omega)) d\Omega \right]}_{F_{abc}(r)} dr. \quad (30)$$

The angular integral in $F_{abc}(r)$ is determined numerically by using the adaptive two-dimensional integration routine **cuhre** from the Cuba 4.2 library [82]. To reduce the number of points at which $F_{abc}(r)$ is evaluated, an adaptive spline interpolation is used, which was developed by us and implemented in our code. Therein, the grid spacing is adjusted such that the absolute error estimate of the interpolation is kept lower than 10^{-6} a.u. on each region with a different spacing. Note that the $F_{abc}(r)$ are determined only once, while the final radial integration in Eq. (30) needs to be evaluated for every transition $i \rightarrow \alpha$. The radial integration in Eq. (30) is carried out using the Simpson rule. For the one-electron continuum-bound integrals that are needed in the evaluation of the one-electron matrix elements in Eq. (19), an analogous approach has been implemented.

V. RESULTS AND DISCUSSION

Here, we perform a thorough benchmark of the approaches to evaluate AES presented in Section II on the exemplary Auger decay of the neon $1s^{-1}3p$ resonance. First, in Section VA, we compare the AES modelled with our protocol against data obtained from an atomic MCDF calculation [64], which serves as a high level theoretical reference. Second, in Section VB, we undertake the comparison to experimental results. The comparison against both theory and experiment is needed since no uniform and highly resolved experimental data covering the full energy range discussed herein has been published to date.

A. Benchmark of theoretical models

Panel (a) of Fig. 2 shows neon AESs, resulting from the autoionization of the $1s^{-1}3p$ states, obtained using bound state wave functions from QC scheme I (cf. Table I) with radial waves corresponding to the spherically averaged direct-exchange potential $V_f^{\text{JX}}(r)$ Eq. (8e). The partial rates have been evaluated using the full \mathcal{H} coupling as well as the approximate r^{-1} coupling in Eq. (19). Further, the nonorthogonality of the continuum and bound orbitals was accounted for by including the conjugate terms, NO, see Eqs. (24, 27). A spectrum employing r^{-1} coupling at the MCDF level, obtained by Stock et al. [64] with the RATIP package [22], serves as a theoretical benchmark. Therein, the atomic structure was obtained with a configuration space including single electron excitations from the $1s$, $2s$, and $2p$ to the np up to $n = 7$ and $3d$ orbitals. The four-component continuum orbitals have been obtained as distorted waves within the potential of the respective ionized atomic state.

All spectra have been constructed by assigning a Gaussian lineshape with an FWHM of $\gamma = 0.1$ eV to each channel.

$$\text{AES}_{1s^{-1}3p}(\varepsilon) = \sum_\alpha \Gamma_{1s^{-1}3p\alpha} G(\varepsilon - \varepsilon_\alpha, \gamma) \quad (31)$$

Where $G(\varepsilon, \gamma) = \sqrt{\ln 2 / (\pi \gamma)} \exp(-4 \ln 2 \varepsilon^2 / \gamma^2)$, ε is the kinetic energy of the emitted electrons and $\varepsilon_\alpha = \mathcal{E}_{1s^{-1}3p} - \mathcal{E}_f$ is the Auger energy of the channel $|\Psi_\alpha\rangle$. The spectra were normalized to the peak height at 811.5 eV, and shifted globally by -5.35 eV (QC I) and -2.45 eV (MCDF) such that the peak at 811.5 eV is aligned to the experimental data taken from Kivimäki et al. [65] (see Fig. 4). In addition, the dominant continuum orbital angular momentum contribution to the intensity is indicated for each peak. This shows that the regions 743 – 765 eV, 765 – 800 eV and 800 – 825 eV correspond almost exclusively to the emission of s , p and d waves, respectively, with the exception that the peak at 803 eV lies in the d -region but is due to s wave emission. Hence, we will refer to this regions as s , p , d rather than using the energies in what follows.

It is evident from Fig. 2 (a) that the normalized AES spectra obtained for the \mathcal{H} and r^{-1} couplings are indistinguishable in the s and d regions and have only very minute differences in the p region. Thus, neglecting the contributions beyond the r^{-1} coupling in the partial rate evaluation is justified in this case. The comparison with the MCDF data in the d region shows that the Auger energies and relative intensities are overall quite well reproduced by our approach. Only the intensities of two small satellite peaks at 803 eV and 809 eV are overestimated and three tiny features around 805.5 – 807.5 eV, are not present using our approach. The latter deficiency can be safely attributed to the smaller configuration space employed in the QC I scheme as compared to the one used to obtain the MCDF results in Ref. 64. Looking at the

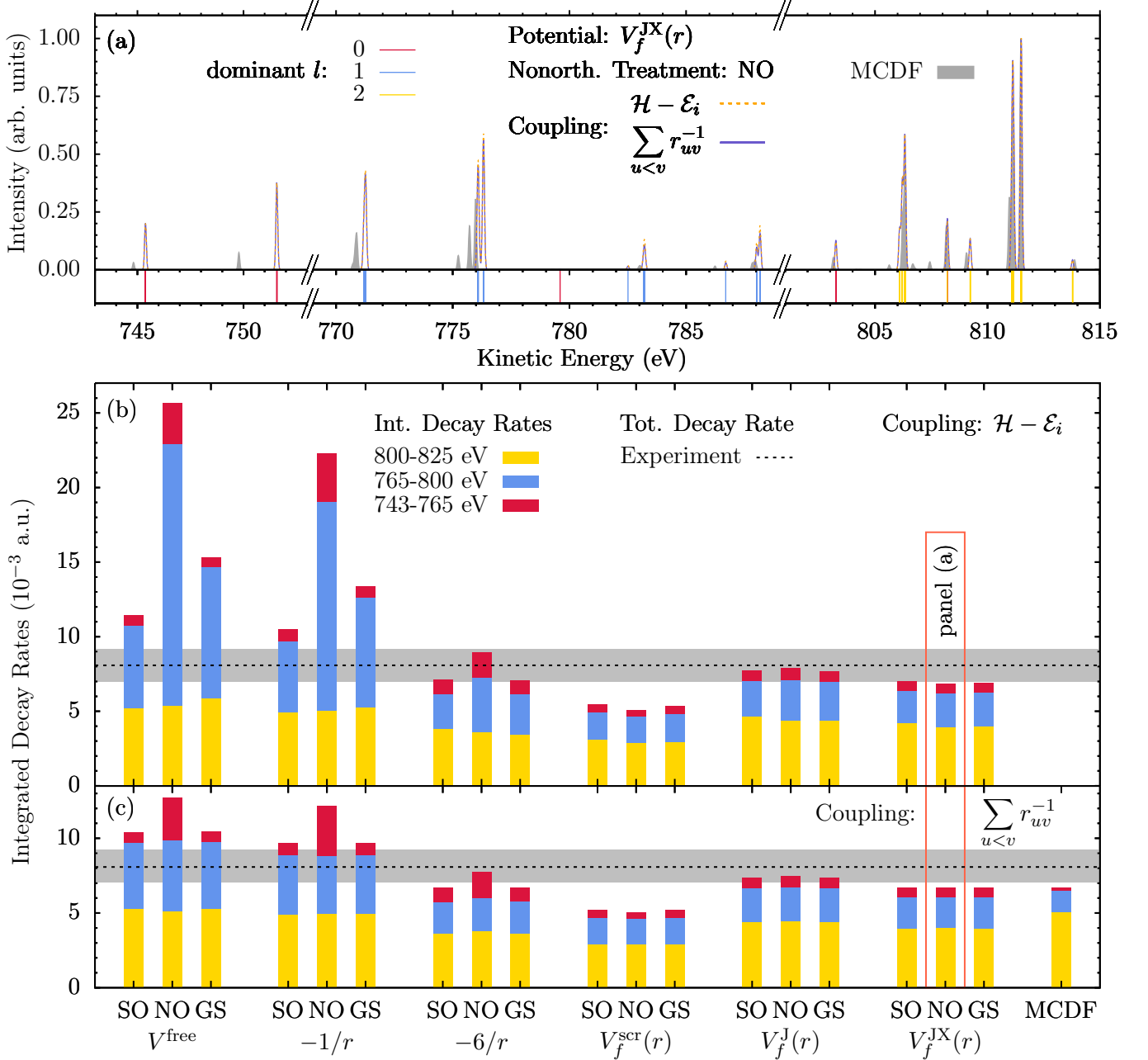


Figure 2. (a) Neon $1s^{-1}3p$ AES obtained with the \mathcal{H} and r^{-1} couplings and the NO approach using continuum orbitals generated by the $V_f^{JX}(r)$ potential are shown in comparison to the MCDF results reported by Stock et al. [64]. All spectra are broadened using a Gaussian profile with an FWHM of 0.1 eV, normalized to the peak at 811.5 eV, and shifted globally to align the 811.5 eV peak with experimental data [65]. The spectra from (a) correspond to the NO histograms of the $V_f^{JX}(r)$ potential in panels (b) and (c). The vertical lines at the bottom of panel (a) indicate the predominant continuum orbital angular momentum (l) contribution to each peak. (b) & (c) Auger decay rates integrated over the given energy ranges corresponding to distinct l contributions. The decay rates have been evaluated based on QC model I for the \mathcal{H} (b) and r^{-1} couplings (c). The radial continuum functions correspond to the depicted potentials. Nonorthogonality of the continuum and bound orbitals was treated with the SO, NO, and GS approaches. The MCDF data have been scaled such that the total decay rate matches the one obtained for the $r^{-1} \cdot V_f^{JX}(r) \cdot \text{NO}$ approach. For reference, the experimentally determined total rate of $8.08 \pm 1.1 \times 10^{-3}$ a.u. (0.22 ± 0.03 eV) [83] is depicted as a horizontal dashed line. The gray region indicates the experimental uncertainty.

s and p regions, the Auger energies from the QC model I become slightly but increasingly blue shifted with respect to the MCDF ones at the lower energy flank of the spectrum. The intensities in turn are considerably overestimated by factors of about two and five for the p and s regions, respectively. Note that very similar spectra are obtained if the RASPT2 energy correction is not used (Supplement: Fig. S1)

Panels (b) and (c) of Fig. 2 show the integrated decay rates for the s , p and d regions evaluated using QC model I with the \mathcal{H} (b) and r^{-1} couplings (c), comparing different approaches to compute the partial decay rates. The rates were obtained for all combinations of potential models in Eqs. (8a - 8e) with the different nonorthogonality approaches SO, NO, and GS for the continuum orbitals. Since no absolute rates for the MCDF results are available, these have been scaled to the total decay rate obtained using the $r^{-1} \cdot V_f^{\text{JX}}(r) \cdot \text{NO}$ treatment. The data in panels (b) and (c) show that the decay rates corresponding to the s , p and d regions converge for both couplings as the quality of the potential is increased from the free particle approximation V^{free} to the spherically averaged direct-exchange potential $V_f^{\text{JX}}(r)$. The $s : p : d$ - ratio obtained from the MCDF spectrum, however, is not matched. Our approaches systematically overestimate the decay rates due to the s and p channels, in line with the mismatch of intensities unveiled in panel (a).

The inclusion of the \mathcal{H} coupling generally leads to larger decay rates. Especially the p region tends to be enhanced in comparison to the r^{-1} coupling results. These effects are very strong for the potentials V^{free} and $-1/r$ and reduce to a slight difference when the more physically sound potentials, $V_f^{\text{scr}}(r)$, $V_f^{\text{J}}(r)$, and $V_f^{\text{JX}}(r)$, are taken. Further, including the conjugate NO terms and using the GS orthogonal continuum waves does not in general improve the results. The NO treatment leads to an overestimation of the partial rates in the s region for the V^{free} , $-1/r$ and $-6/r$ potentials. Moreover, in conjunction with the \mathcal{H} coupling it enhances the already present overestimation of the decay rates in the p region for these potentials. Notably, this is partially cured by using the GS approach on top of \mathcal{H} coupling. This is in contrast to using GS together with the r^{-1} coupling, where one obtains the same results as with the SO approximation. Interestingly, the choice of the nonorthogonality treatment has only a weak influence on the decay rate distribution, when either of the $V_f^{\text{scr}}(r)$, $V_f^{\text{J}}(r)$, or $V_f^{\text{JX}}(r)$ potentials is used. Roughly, this can be attributed to the magnitude of the bound-continuum orbital overlap that decreases if the potential is chosen to be more realistic. Hence, leading to a negligible effect of the conjugate terms in Eqs. (24, 27) and the GS orthogonalization for these potentials.

We conclude the discussion of this figure with the observation that only the total rates obtained with the $-6/r$, $V_f^{\text{J}}(r)$, and $V_f^{\text{JX}}(r)$ potentials reproduce the experimentally observed decay rate [83]. The best match is obtained with the $V_f^{\text{J}}(r)$ potential, whereas the $V_f^{\text{JX}}(r)$

leads to slightly underestimated total rates, which can be attributed to the inclusion of the attractive exchange term, Eq. (13). Similarly, we assign the considerable underestimation of the total decay rates by the $V_f^{\text{scr}}(r)$ potential to the fact that it is more attractive in the core region than $V_f^{\text{JX}}(r)$, see Fig. 3. The V^{free} model always leads to overestimated total rates and the $-1/r$ potential yields satisfactory total rates only when combined with the SO or GS approaches. However, despite the good agreement in the total rates the spectra for the $r^{-1} \cdot -1/r \cdot \text{SO}$ approach deviate considerably from the ones obtained for the more accurate potentials (Supplement: Fig. S4), indicating that this agreement is rather accidental.

To shed light on the sensitivity of the decay rates obtained with QC model I, \mathcal{H} coupling, and the NO approach, the influence of different potential models on the radial continuum functions and the spectra is presented in Fig. 3. Panel (a) contains the normalized AESs obtained using the potentials $-1/r$, $-6/r$, $V_f^{\text{scr}}(r)$, and $V_f^{\text{JX}}(r)$. Shifts and broadening parameters are the same as in Fig. 2 (a). The d region is represented very well with all potential models, with the exclusion that the satellite bands at 803 eV and 808 eV are barely present when using the $-1/r$ potential. In contrast, the relative intensities of the s and p regions of the spectra are strongly affected by the choice of the potential. Here, the p region comprises two peak groups with different character. When using the effective Coulomb potentials, the peaks around 771 eV and 776 eV are overestimated by at most a factor of two with respect to the $V_f^{\text{JX}}(r)$ potential. In contrast, the satellite bands around 783 eV and 787 eV are overestimated by an order of magnitude when using the $-1/r$ potential. This behavior can be attributed to the presence of both: one-electron Hamiltonian coupling terms and the conjugate NO terms, leading to an enhancement of the error introduced by the potential. In turn, the screening potential model slightly overestimates the former and underestimates the latter group of peaks. Finally, the spectra obtained with $V_f^{\text{scr}}(r)$ and $V_f^{\text{JX}}(r)$ are indistinguishable in the s regions, but using $-1/r$ and $-6/r$ leads to strongly overestimated intensities. In accord with the data shown in Fig. 2, this is due to the NO treatment. To underline this conclusion the SO spectra for the \mathcal{H} and r^{-1} couplings are shown in the Supplement as Figs. S3 and S4.

For each region, the radial waves and respective potentials, including the angular momentum term, are shown in the panels (b-d) corresponding to the characteristic peaks denoted in panel (a). Note that the V^{free} and $V_f^{\text{J}}(r)$ cases are very similar to $-1/r$ and $V_f^{\text{JX}}(r)$, respectively. Thus, they are not shown in Fig. 3 and have been excluded from the discussion of this figure. One might understand the differences in the sensitivity of the s , p and d regions to the potential model by comparing the short range behavior of the radial waves $w_l^{fk}(r)/r$, Eq. (17a), with the electron density that is sharply peaked in the

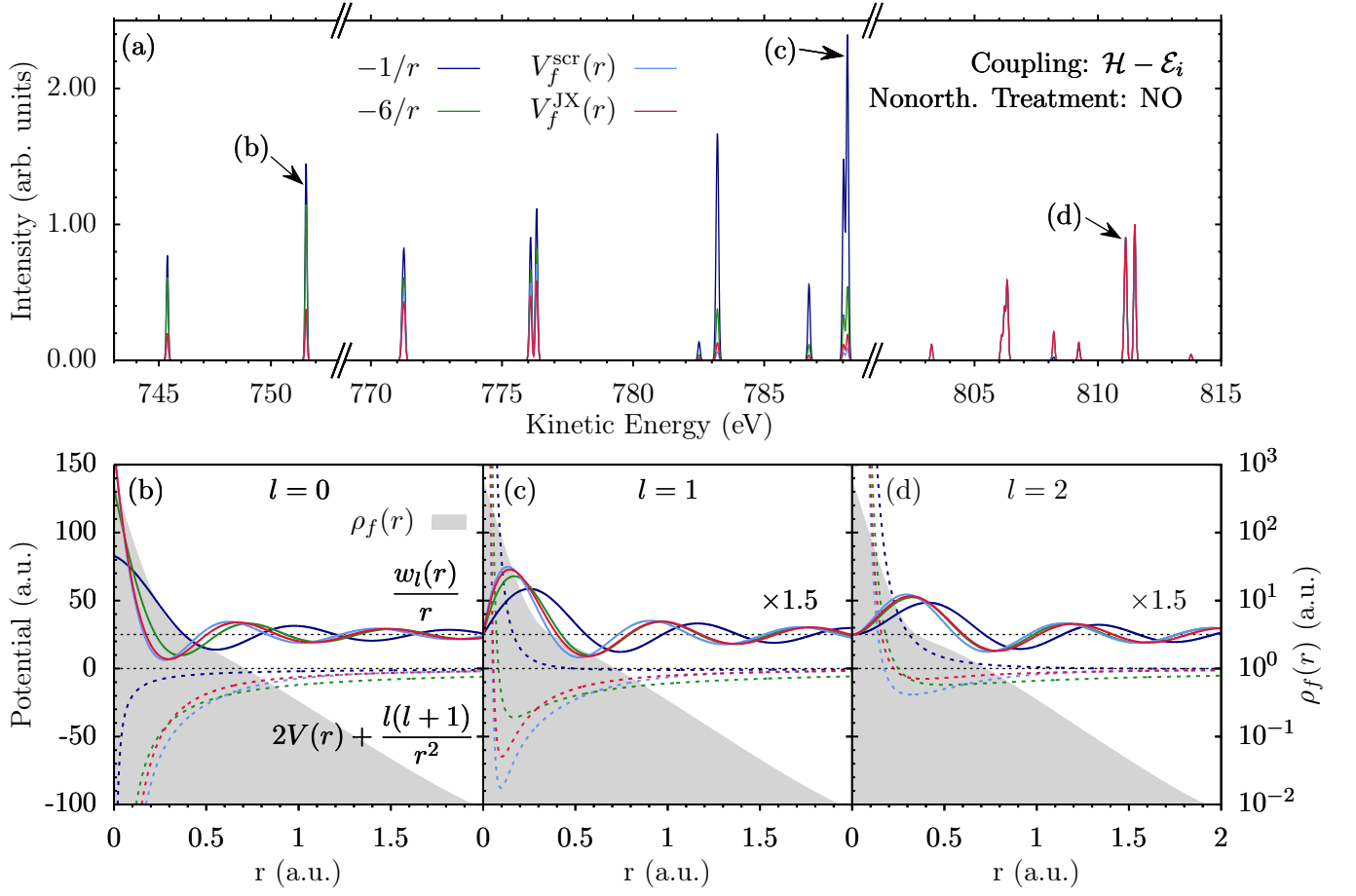


Figure 3. (a) Neon $1s^{-1}3p$ AES evaluated using QC scheme I, \mathcal{H} coupling, and the NO nonorthogonality treatment with radial continuum functions corresponding to the given potentials. The spectra are normalized to the peak at 811.5 eV, broadened using a Gaussian FWHM of 0.1 eV and shifted globally by -5.35 eV. (b-d) Effective radial potentials (dashed) and continuum functions (solid) corresponding to the dominant angular momentum contribution $l = 0, 1, 2$ of the peaks (b-d) in panel (a) are shown together with the spherically averaged electron densities $\rho_f(r)$ of the respective ionized states. The colors of the radial waves and potentials correspond to the spectra shown in panel (a).

core region. This suggests that the matrix elements in Eq. (19) are very sensitive to the description of the continuum orbitals in this region. It is well known that only the s waves have a considerable contribution at the core, while the radial functions tend to zero as r^l otherwise. In fact, the effective radial potential at the core is dominated by the angular momentum term for $l > 0$, meaning that the influence of the present potential models on the total rates should decrease with increasing l . In contrast to this simple argumentation, the p region is more sensitive to variations in the potential model than the s region, even when r^{-1} coupling and the SO approximation are considered, Fig 2 (c). In fact, for the s waves it is seen that only the potentials $V_f^{\text{scr}}(r)$ and $V_f^{\text{JX}}(r)$ lead to similar radial waves, the slight differences being due to the fact that the screening model is too attractive in the core region. Notably, these slight deviations lead to an underestimation of the total decay rates obtained with the $V_f^{\text{scr}}(r)$ potential by about 25% in comparison to

those obtained for $V_f^{\text{JX}}(r)$ (see Fig. 2), underlining the sensitivity of the total decay rates to the choice of the model potential.

The effective Coulomb potential $-1/r$ provides a qualitatively wrong description in both, the core and outer regions, whereas the $-6/r$ potential leads to a sort of compromise in accuracy. It describes the core region much better than the $-1/r$ potential but as a trade off has a wrong asymptotic behavior in the valence region. Still, the accuracy is not enough to describe the intensities in the s region when the conjugate terms are included, due to wrong overlaps with the bound orbitals. However, the p and d continuum waves obtained with the $-6/r$ potential are similar to the ones obtained with the more accurate potentials (in the plotted range). This is reflected in the better description of intensities in the p and d regions. Notably, the spectra obtained with $-6/r$ using either \mathcal{H} or r^{-1} coupling in the SO approximation, agree qualitatively with the ones obtained for the more accurate potentials (Supplement: Figs. S3 and S4). Thus,

one can conclude that using the SO approximation provides some sort of error cancellation mechanism for the considered cases. Finally, the use of the $-1/r$ potential is only justified for the main features of the d region. If one is interested in the full spectrum, one should use a model taking into account the electronic potential of the ionized core, such as $V_f^{\text{scr}}(r)$, $V_f^{\text{J}}(r)$ or $V_f^{\text{JX}}(r)$. Generally, special caution has to be taken when \mathcal{H} coupling and the NO approach are used together with simple potential models. Despite the formally more correct treatment, the combination with such potentials produces results that are in bad agreement with the MCDF data.

Summarizing the discussion until this point, it seems that satisfactory total decay rates and AES are only obtained with the potentials $V_f^{\text{J}}(r)$ and $V_f^{\text{JX}}(r)$. Further, employing r^{-1} coupling and the SO approximation seems to be very well justified for this case and we will use these in the comparison against experimental data below.

B. Comparison to experimental data

In this section, the comparison of our theoretical results to the experimental data in the full spectral range is presented. In addition, to unravel the influence of the underlying QC onto the AES, we discuss spectra obtained with the QC schemes I-III as described in Table I. The QC model II, which is more sophisticated than QC I, contains an uncontracted s basis and accounts for scalar relativistic effects, whereas III employs an active space larger than in QC I.

To the best of our knowledge, no experimental Auger emission spectrum of the neon $1s^{-1}3p$ resonance that covers the full spectral range presented in Figs. 2 and 3 has been published to date. Hence, in Fig. 4 the spectra obtained with the QC models I-III and the $r^{-1} \cdot V_f^{\text{JX}}(r) \cdot \text{SO}$ approach are compared against experimental data taken from Kivimäki et al. [65], for the d region (a), and Yoshida et al. [66], for the s and p regions (b). The spectra have been shifted by -5.35 eV, -4.75 eV, and -5.18 eV for QC models I, II, and III to align the peaks at 811.5 eV. In panel (a), the spectra have been broadened using a Gaussian profile with an FWHM of 0.25 eV, corresponding to the lineshape of the peak at 806.5 eV in the experimental spectrum. Further, in panel (b) a Gaussian FWHM of 0.77 eV was chosen such as to represent the HWHM of the high energy flank of the peak at 778.5 eV in the experimental spectrum. Additionally, the spectra have been normalized to the heights of the main peaks at 811.5 eV (a) and 776 eV (b). Finally, the experimental data have been recorded at angles of 54.7° (a) and 56° (b) to the polarization vector. Data for these angles has been chosen to rule out anisotropy effects which makes the comparison with our angle integrated spectra easier.

Panel (a) shows that the agreement between the experimental and the theoretical spectra is fairly good. In fact, the relative energetic positions and intensities of the

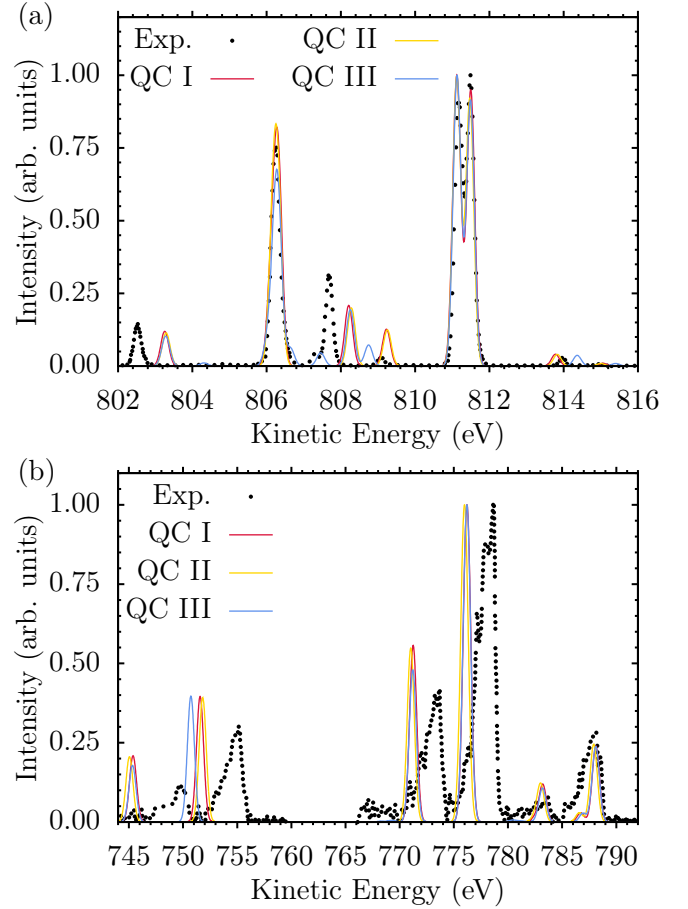


Figure 4. Comparison of experimental and theoretical neon $1s^{-1}3p$ AES obtained based on the QC schemes I - III with the $r^{-1} \cdot V_f^{\text{JX}}(r) \cdot \text{SO}$ method. The spectra obtained with QC I, II, and III have been shifted by -5.35 eV, -4.75 eV, and -5.18 eV, respectively, to align the peak at 811.5 eV with the experimental data in panel (a). To account for the different lineshapes of the experimental spectra that have been digitalized from [65], panel (a), and [66] in panel (b), broadening with a Gaussian FWHM of 0.25 eV and 0.77 eV was used in panels (a) and (b), respectively. Further, the spectra have been normalized individually to the peaks at 811.5 eV (a) and 776 eV (b).

main peaks are reproduced quite well. However, smaller satellite peaks at 803 eV and 808.2 eV are blue shifted by about 0.5 eV. Generally, the agreement between theory and experiment is worse for the smaller features, although an unambiguous assignment is still possible. Using the uncontracted s basis and including scalar relativistic effects in QC II does not influence the resulting spectrum. In turn, the larger active space incorporated in the QC scheme III leads to a better reproduction of some tiny features at 806.4 eV, 807.5 eV and 808.8 eV. The blue shifts of the peaks already present with QC I and II are not affected, when employing QC III.

The comparison of the spectra covering the s and p regions with the experimental data is shown in panel (b). Here, the overall agreement is worse than in panel (a)

both concerning the relative intensities and energetic positions of the peaks. Specifically, the positions of the peaks around 783 eV and 788 eV are reproduced well by all methods, while the intensities of the former and latter peaks are slightly over- and underestimated, respectively. Further, the peaks at 771 eV and 776 eV are red shifted by about 2 eV, and the relative intensity of the former is overestimated by approximately 30% (QC I and II) and 20% (QC III). Finally, the peaks at 745 eV and around 751 eV, corresponding to the s region are redshifted by 5 eV (QC I-III) and 4 eV (QC I, II), or 5 eV (QC III), respectively. The intensities of these peaks are overestimated by about 30% with respect to the experimental data. Consequently, this means that the s region is overestimated only by approximately 30% with respect to the p region. In fact, this is considerably less than what was suggested by the comparison with the MCDF spectrum in Fig. 2. The total decay rates, however, are not visibly altered by the choice of either of the QC schemes I, II or III (cf. Supplement: Fig. S5).

To wrap up this discussion, we conclude that the RASSCF/RASPT2 electronic structure method combined with the $r^{-1} \cdot V_f^{\text{JX}} \cdot \text{SO}$ approach to construct continuum orbitals and evaluate the transition matrix elements provides Auger energies and intensities for the decay of the neon $1s^{-1}3p$ resonance of a similar quality as those obtained in Ref. 64 with the MCDF approach. In particular, a straightforward assignment of experimental results is possible. Further, the inclusion of scalar relativistic effects into the one-component electronic structure of the bound states has no notable influence on the spectra, while a large active space is necessary only to reproduce minor satellite features.

VI. CONCLUSIONS AND OUTLOOK

In this work, we have demonstrated an approach to the evaluation of autoionization rates on the example of the Auger decay from the neon $1s^{-1}3p$ resonance. The suggested protocol is based on the RASSCF/RASPT2 method to evaluate the bound state wave functions and energies, supplemented by a single-channel scattering model for the outgoing electron. Here, the single-center approximation is introduced to reduce the continuum orbital problem to the radial dimension by averaging over the angular structure of the ionized electron density. To model the true radial potential, six different models, V^{free} , $-1/r$, $-6/r$, $V_f^{\text{scr}}(r)$, $V_f^{\text{J}}(r)$, and $V_f^{\text{JX}}(r)$, have been discussed. Further, three different ways to account for the nonorthogonality of the continuum and bound orbitals, SO, NO, and GS, as well as the effect of using complete, \mathcal{H} , or approximate, r^{-1} , coupling in the partial rate evaluation has been investigated. All combinations of these sum up to 36 different variants to evaluate partial autoionization rates for an underlying bound state QC calculation and have been implemented in a standalone program.

Here we compared all these approaches with respect to their ability to reproduce the experimental [65, 66] as well as theoretical AES obtained at the fully relativistic MCDF level [64]. We showed that the Auger energies obtained with a Rydberg basis set and an active space allowing single electron excitations into the $3s$, $3p$, $4s$, and $4p$ orbitals are generally in good agreement with the theoretical reference. However, the quality of the continuum orbital was shown to be the most important issue as it strongly influences the obtained AESs. Especially the core region must be described well by any potential that is used in the evaluation of AES. For instance, we found that the d region of the spectrum is rather insensitive to the choice of the model potential, whereas the s and p regions require to use one of the potentials $V_f^{\text{scr}}(r)$, $V_f^{\text{J}}(r)$ and $V_f^{\text{JX}}(r)$. Still, the MCDF intensities can only be reproduced in the d region of the spectrum, while they are overestimated in the s and p parts. Further, the free particle model and the asymptotic Coulomb potential $-1/r$ fail to reproduce the complete spectrum. Interestingly, inclusion of the full \mathcal{H} coupling as well as the NO or GS terms in addition to using r^{-1} coupling in the SO approximation does not in general lead to improved spectra, but rather emphasizes the deficiencies of the V^{free} , $-1/r$ and $-6/r$ potentials. With the SO approximation, however, the effective $-6/r$ potential already leads to qualitative agreement with the spectra obtained using the more accurate potentials. In contrast, the spectra obtained with $V_f^{\text{scr}}(r)$, $V_f^{\text{J}}(r)$ and $V_f^{\text{JX}}(r)$, are weakly affected by the choice of both the coupling and nonorthogonality approaches. These findings suggest that the SO approximation as well as the r^{-1} coupling provide a means of error cancellation in the evaluation of partial decay rates.

The comparison with experimentally obtained spectra using the $r^{-1} \cdot V_f^{\text{JX}}(r) \cdot \text{SO}$ approach demonstrated the ability of the present method to accurately predict the neon $1s^{-1}3p$ AES, allowing a straightforward assignment of the experimental data. Interestingly, the general structure of the spectrum can be already reproduced quite well using a rather small active space, and is not sensitive to the inclusion of scalar relativistic effects. The best agreement with the experimental data is achieved by using a larger active space, including additional excitations to $3d$, $5s$, $5p$, $6s$, and $6p$ orbitals together with the spherically averaged direct exchange potential $V_f^{\text{JX}}(r)$. In addition, our approach can successfully reproduce the experimentally measured total decay rate of the neon $1s^{-1}3p$ resonance, when the potentials $-6/r$ (only in SO), $V_f^{\text{J}}(r)$, and $V_f^{\text{JX}}(r)$ are used. Since using the screened charge potential $V_f^{\text{scr}}(r)$ leads to notably underestimated absolute rates and is not computationally cheaper than using either $V_f^{\text{J}}(r)$ or $V_f^{\text{JX}}(r)$, providing a better accuracy, we suggest to disregard the $V_f^{\text{scr}}(r)$ potential for the evaluation of Auger emission rates.

Molecular systems can be treated with the presented method as well, however, in this case the one-center model has to be adopted, leading to a much more approx-

imate representation of the molecular continuum than in the atomic case. To keep the errors due to this approximation as small as possible, our findings suggest to use the r^{-1} coupling together with the SO approximation to evaluate molecular AIS. The potentials should be modeled using either the direct $V_f^J(r)$ or direct-exchange $V_f^{JX}(r)$ variant. The applicability of these approximations has to be tested for the molecular case.

Currently our code is interfaced to the MOLCAS/openMolcas as well as to the Gaussian program packages, allowing to evaluate PES and AIS based on bound state calculations conducted with the RASSCF/RASPT2 [61], as well as the linear-response time-dependent density functional theory method [84]. A publication discussing the applicability of the present

models to treat molecular systems is in preparation. The extension of the approach to evaluate angular resolved spectra is straight-forward and will be considered in future works.

ACKNOWLEDGMENTS

We would like to thank Prof. Dr. Stephan Fritzsche, from the Helmholtz Institute Jena, Randolph Beerwerth and Sebastian Stock from his group for fruitful discussions and for providing the unshifted results of the MCDF calculations from Ref. 64. Financial support from the Deutsche Forschungsgemeinschaft Grant No. BO 4915/1-1 is gratefully acknowledged.

-
- [1] V. G. Wentzel, Z. Physik **43**, 524 (1927).
 - [2] P. Van der Heide, *X-Ray Photoelectron Spectroscopy: An Introduction to Principles and Practices* (Wiley, Hoboken, N.J., 2012).
 - [3] S. Hofmann, *Auger- and X-Ray Photoelectron Spectroscopy in Materials Science: A User-Oriented Guide*, Springer Series in Surface Sciences No. 49 (Springer, Heidelberg, New York, 2013).
 - [4] S. Hüfner, *Photoelectron Spectroscopy: Principles and Applications* (Springer, Berlin, Heidelberg, 2003).
 - [5] L. Meitner, Z. Physik **11**, 35 (1922).
 - [6] L. S. Cederbaum, J. Zobeley, and F. Tarantelli, Phys. Rev. Lett. **79**, 4778 (1997).
 - [7] J. Zobeley, R. Santra, and L. S. Cederbaum, J. Chem. Phys. **115**, 5076 (2001).
 - [8] P. Slavíček, N. V. Kryzhevoi, E. F. Aziz, and B. Winter, J. Phys. Chem. Lett. **7**, 234 (2016).
 - [9] P. Slavíček, B. Winter, L. S. Cederbaum, and N. V. Kryzhevoi, J. Am. Chem. Soc. **136**, 18170 (2014).
 - [10] M. A. Brown, M. Faubel, and B. Winter, Annu. Rep. Sect. C Phys. Chem. **105**, 174 (2009).
 - [11] V. Stumpf, K. Gokhberg, and L. S. Cederbaum, Nat. Chem. **8**, 237 (2016).
 - [12] H. Wang, T. Möhle, O. Kühn, and S. I. Bokarev, Phys. Rev. A **98**, 013408 (2018).
 - [13] F. de Groot and A. Kotani, *Core Level Spectroscopy of Solids* (CRC Press, Boca Raton, 2008).
 - [14] R. W. Howell, Int. J. Radiat. Biol. **84**, 959 (2008).
 - [15] E. Alizadeh, T. M. Orlando, and L. Sanche, Annu. Rev. Phys. Chem. **66**, 379 (2015).
 - [16] R. F. Martin and L. E. Feinendegen, Int. J. Radiat. Biol. **92**, 617 (2016).
 - [17] A. Yokoya and T. Ito, Int. J. Radiat. Biol. **93**, 743 (2017).
 - [18] R. Neutze, R. Wouts, D. van der Spoel, E. Weckert, and J. Hajdu, Nature **406**, 752 (2000).
 - [19] T. Åberg and G. Howat, in *Corpsucles and Radiation in Matter I*, Encyclopedia of Physics, Vol. 31, edited by W. Mehlhorn (Springer, Berlin, 1982) p. 469.
 - [20] T. Åberg, Phys. Scr. **21**, 495 (1980).
 - [21] U. Fano, Phys. Rev. **124**, 1866 (1961).
 - [22] S. Fritzsche, Comput. Phys. Commun. **183**, 1525 (2012).
 - [23] H. Ågren, S. Svensson, and U. Wahlgren, Chem. Phys. Lett. **35**, 336 (1975).
 - [24] H. Ågren, J. Chem. Phys. **75**, 1267 (1981).
 - [25] I. Hillier and J. Kendrick, Mol. Phys. **31**, 849 (1976).
 - [26] M. Mitani, O. Takahashi, K. Saito, and S. Iwata, J. Electron Spectrosc. Relat. Phenom. **128**, 103 (2003).
 - [27] V. Carravetta, H. Ågren, O. Vahtras, and H. J. A. Jensen, J. Chem. Phys. **113**, 7790 (2000).
 - [28] B. Schimmelpfennig, B. Nestmann, and S. D. Peyerimhoff, J. Phys. B At. Mol. Opt. Phys. **25**, 1217 (1992).
 - [29] B. Schimmelpfennig, B. Nestmann, and S. Peyerimhoff, J. Electron Spectrosc. Relat. Phenom. **74**, 173 (1995).
 - [30] J. Oddershede, in *Advances in Chemical Physics*, edited by K. P. Lawley (John Wiley & Sons, Inc., Hoboken, NJ, USA, 1987) pp. 201–239.
 - [31] C.-M. Liegener, Chem. Phys. Lett. **90**, 188 (1982).
 - [32] V. Averbukh and L. S. Cederbaum, J. Chem. Phys. **123**, 204107 (2005).
 - [33] P. Kolorenč, V. Averbukh, K. Gokhberg, and L. S. Cederbaum, J. Chem. Phys. **129**, 244102 (2008).
 - [34] P. Kolorenč and V. Averbukh, J. Chem. Phys. **135**, 134314 (2011).
 - [35] H. Siegbahn, L. Asplund, and P. Kelfve, Chem. Phys. Lett. **35**, 330 (1975).
 - [36] D. R. Jennison, Chem. Phys. Lett. **69**, 435 (1980).
 - [37] F. P. Larkins, L. C. Tulea, and E. Z. Chelkowska, Aust. J. Phys. **43**, 625 (1990).
 - [38] R. Fink, J. Electron Spectrosc. Relat. Phenom. **76**, 295 (1995).
 - [39] O. Travnikova, R. F. Fink, A. Kivimäki, D. Céolin, Z. Bao, and M. N. Piancastelli, Chem. Phys. Lett. **474**, 67 (2009).
 - [40] L. Inhester, K. Hanasaki, Y. Hao, S.-K. Son, and R. Santra, Phys. Rev. A **94** (2016).
 - [41] Y. Hao, L. Inhester, K. Hansaki, and R. Santra, Struct. Dyn. **2**, 041707 (2015).
 - [42] K. Faegri and H. P. Kelly, Phys. Rev. A **19**, 1649 (1979).
 - [43] M. Higashi, E. Hiroike, and T. Nakajima, Chem. Phys. **68**, 377 (1982).
 - [44] K. Zähringer, H.-D. Meyer, and L. S. Cederbaum, Phys. Rev. A **45**, 318 (1992).
 - [45] P. V. Demekhin, D. V. Omel'yanenko, B. M. Lagutin, V. L. Sukhorukov, L. Werner, A. Ehresmann, K.-H. Scharner, and H. Schmoranzner, Opt. Spectrosc. **102**, 318 (2007).

- [46] P. V. Demekhin, I. D. Petrov, V. L. Sukhorukov, W. Kielich, P. Reiss, R. Hentges, I. Haar, H. Schmoranzner, and A. Ehresmann, *Phys. Rev. A* **80** (2009).
- [47] R. Colle and S. Simonucci, *Phys. Rev. A* **39**, 6247 (1989).
- [48] R. Colle and S. Simonucci, *Phys. Rev. A* **48**, 392 (1993).
- [49] R. Colle, D. Embriaco, M. Massini, S. Simonucci, and S. Taioli, *J. Phys. B At. Mol. Opt. Phys.* **37**, 1237 (2004).
- [50] C. Marante, M. Klinker, I. Corral, J. González-Vázquez, L. Argenti, and F. Martín, *J. Chem. Theor. Comp.* **13**, 499 (2017).
- [51] C. Marante, M. Klinker, T. Kjellsson, E. Lindroth, J. González-Vázquez, L. Argenti, and F. Martín, *Phys. Rev. A* **96** (2017).
- [52] M. Klinker, C. Marante, L. Argenti, J. González-Vázquez, and F. Martín, *Phys. Rev. A* **98** (2018).
- [53] J. V. Ortiz, *J. Chem. Phys.* **81**, 5873 (1984).
- [54] N. Correia, A. Naves de Brito, M. P. Keane, L. Karlsson, S. Svensson, C.-M. Liegener, A. Cesar, and H. Ågren, *J. Chem. Phys.* **95**, 5187 (1991).
- [55] K. Endo, S. Shimada, N. Kato, and T. Ida, *J. Mol. Struct.* **1122**, 341 (2016).
- [56] P. G. Burke, *R-Matrix Theory of Atomic Collisions: Application to Atomic, Molecular and Optical Processes*, Springer Series on Atomic, Optical, and Plasma Physics No. 61 (Springer, Heidelberg, 2011).
- [57] S. I. Bokarev, M. Dantz, E. Suljoti, O. Kühn, and E. F. Aziz, *Phys. Rev. Lett.* **111**, 083002 (2013).
- [58] R. V. Pinjari, M. G. Delcey, M. Guo, M. Odelius, and M. Lundberg, *J. Comput. Chem.* **37**, 477 (2016).
- [59] I. Josefsson, K. Kunnus, S. Schreck, A. Föhlisch, F. de Groot, P. Wernet, and M. Odelius, *J. Phys. Chem. Lett.* **3**, 3565 (2012).
- [60] S. I. Bokarev, M. Khan, M. K. Abdel-Latif, J. Xiao, R. Hilal, S. G. Aziz, E. F. Aziz, and O. Kühn, *J. Phys. Chem. C* **119**, 19192 (2015).
- [61] G. Grell, S. I. Bokarev, B. Winter, R. Seidel, E. F. Aziz, S. G. Aziz, and O. Kühn, *J. Chem. Phys.* **143**, 074104 (2015).
- [62] R. Golnak, S. I. Bokarev, R. Seidel, J. Xiao, G. Grell, K. Atak, I. Unger, S. Thürmer, S. G. Aziz, O. Kühn, B. Winter, and E. F. Aziz, *Sci. Rep.* **6**, 24659 (2016).
- [63] J. Norell, G. Grell, O. Kühn, M. Odelius, and S. I. Bokarev, *Phys. Chem. Chem. Phys.* **20**, 19916 (2018).
- [64] S. Stock, R. Beerwerth, and S. Fritzsche, *Phys. Rev. A* **95** (2017).
- [65] A. Kivimäki, S. Heinäsmäki, M. Jurvansuu, S. Alitalo, E. Nömmiste, H. Aksela, and S. Aksela, *J. Electron Spectrosc. Relat. Phenom.* **114**, 49 (2001).
- [66] H. Yoshida, K. Ueda, N. M. Kabachnik, Y. Shimizu, Y. Senba, Y. Tamenori, H. Ohashi, I. Koyano, I. H. Suzuki, R. Hentges, J. Vieffhaus, and U. Becker, *J. Phys. B At. Mol. Opt. Phys.* **33**, 4343 (2000).
- [67] K. Ueda, M. Kitajima, A. De Fanis, Y. Tamenori, H. Yamaoka, H. Shindo, T. Furuta, T. Tanaka, H. Tanaka, H. Yoshida, R. Sankari, S. Aksela, S. Fritzsche, and N. M. Kabachnik, *Phys. Rev. Lett.* **90** (2003).
- [68] Y. Tamenori and I. H. Suzuki, *J. Phys. B At. Mol. Opt. Phys.* **47**, 145001 (2014).
- [69] J. C. Slater, *Phys. Rev.* **81**, 385 (1951).
- [70] F. W. J. Olver, D. W. Lozier, R. F. Boisvert, and C. W. Clark, eds., *NIST Handbook of Mathematical Functions*, 1st ed. (Cambridge University Press, 2010).
- [71] P.-O. Löwdin, *Phys. Rev.* **97**, 1474 (1955).
- [72] F. Aquilante, J. Autschbach, R. K. Carlson, L. F. Chibotaru, M. G. Delcey, L. De Vico, I. F. Galván, N. Ferré, L. M. Frutos, L. Gagliardi, M. Garavelli, A. Giussani, C. E. Hoyer, G. Li Manni, H. Lischka, D. Ma, P. Å. Malmqvist, T. Müller, A. Nenov, M. Olivucci, T. B. Pedersen, D. Peng, F. Plasser, B. Pritchard, M. Reiher, I. Rivalta, I. Schapiro, J. Segarra-Martí, M. Stenrup, D. G. Truhlar, L. Ungur, A. Valentini, S. Vancollie, V. Veryazov, V. P. Vysotskiy, O. Weingart, F. Zapata, and R. Lindh, *J. Comput. Chem.* **37**, 506 (2016).
- [73] P.-O. Widmark, P. Å. Malmqvist, and B. O. Roos, *Theor. Chim. Acta* **77**, 291 (1990).
- [74] K. Kaufmann, W. Baumeister, and M. Jungen, *J. Phys. B At. Mol. Opt. Phys.* **22**, 2223 (1989).
- [75] J. Almlöf and P. R. Taylor, *J. Chem. Phys.* **86**, 4070 (1987).
- [76] *openMolcas* (<https://gitlab.com/Molcas/OpenMolcas>, 2018).
- [77] D. Peng and M. Reiher, *Theor. Chem. Acc.* **131** (2012).
- [78] P. Å. Malmqvist, K. Pierloot, A. R. M. Shahi, C. J. Cramer, and L. Gagliardi, *J. Chem. Phys.* **128**, 204109 (2008).
- [79] P. Å. Malmqvist, B. O. Roos, and B. Schimmelpfennig, *Chem. Phys. Lett.* **357**, 230 (2002).
- [80] P. Å. Malmqvist, *Int. J. Quantum Chem.* **30**, 479 (1986).
- [81] Q. Sun, *J. Comput. Chem.* **36**, 1664 (2015).
- [82] T. Hahn, *Comput. Phys. Commun.* **168**, 78 (2005).
- [83] L. Avaldi, G. Dawber, R. Camilloni, G. C. King, M. Roper, M. R. F. Siggel, G. Stefani, M. Zitnik, A. Lisini, and P. Decleva, *Phys. Rev. A* **51**, 5025 (1995).
- [84] T. Möhle, O. S. Bokareva, G. Grell, O. Kühn, and S. I. Bokarev, *J. Chem. Theory Comput.* **14**, 5870 (2018).